Force, Surface Pressure, and Flowfield Measurements on a Slender Missile Configuration with Square Cross-Section at Supersonic Speeds

Floyd J. Wilcox, Jr.*
NASA Langley Research Center, Hampton, Va. 23681

Trevor J. Birch†
Dstl, Bedford, UK

and

Jerry M. Allen‡
NASA Langley Research Center, Hampton, Va. 23681

A wind-tunnel investigation of a square cross-section missile configuration has been conducted to obtain force and moment measurements, surface pressure measurements, and vapor screen flow visualization photographs for comparison with computational fluid dynamics studies conducted under the auspices of The Technical Cooperation Program (TTCP). Tests were conducted on three configurations which included: (1) body alone, (2) body plus tail fins mounted on the missile corners, and (3) body plus tail fins mounted on the missile side. This test was conducted in test section #2 of the NASA Langley Unitary Plan Wind Tunnel at Mach numbers of 2.50 and 4.50 and at a Reynolds number of 4 million per ft. The data were obtained over an angle of attack range from -4° to 24° and roll angles from 0° to 45°, i.e., from a diamond shape (as viewed from the rear) at a roll angle of 0° to a square shape at 45°.

Nomenclature

Symbols:

A	=	reference area, 0.074667 ft^2
C_A	=	axial force coefficient, AF/(qA)
C_l	=	rolling moment coefficient, RM/(qAD)
C_m	=	pitching moment coefficient, PM/(qAD)
C_N	=	normal force coefficient, NF/(qA)
C_n	=	yawing moment coefficient, YM/(qAD)
C_p	=	pressure coefficient, $(p-p_\infty)/q$
C_Y	=	side force coefficient, SF/(qA)
D	=	length of square cross-section side (reference length), 3.70 in
q	=	dynamic pressure, lb/ft^2
L	=	missile length, 48.10 in.
M	=	Mach number

* Aerospace Engineer
† Leader, Air Vehicle Technology, Senior Member AIAA
‡ Senior Aerospace Engineer, Associate Fellow AIAA

p = static pressure, lb/ft^2
p_o = stagnation pressure, lb/ft^2
p_∞ = free stream static pressure, lb/ft^2
q = free stream dynamic pressure, lb/ft^2
Re = Reynolds number, per ft
T_0 = stagnation temperature, °F
x = Cartesian coordinate, in.
α = angle of attack, deg
θ = azimuth angle indicating pressure orifice location, deg
ϕ = model roll angle, deg

Abbreviations:
AF = axial force, lb
NF = normal force, lb
MS = model station, in.
PM = pitching moment, in-lb
RM = rolling moment, in-lb
SF = side force, lb
YM = yawing moment, in-lb

I. Introduction

Computational fluid dynamics (CFD) has become an integral part of aerospace vehicle design. In many instances, CFD can produce results which are quite accurate. However, for missiles at moderate to high angles of attack, the flow field can become quite complicated with regions of flow separation and body and wing vortices. Before relying on CFD codes to predict the aerodynamic performance of missiles with these complicated flow fields, it is important to validate the codes with reliable experimental data.

Recently, the Conventional Weapons Technology Group (WPN) of The Technical Cooperation Program (TTCP) sponsored a study (Key Task 2-15) to evaluate the ability of various CFD codes to compute the aerodynamic characteristics of a slender axisymmetric missile configuration[1-6]. A follow-on study (Key Task 2-19) was approved by TTCP to evaluate the ability of various CFD codes to compute the flow fields about three non-axisymmetric missile configurations[7-12]. Two of these configurations were based on a square cross-section body and the final case was based on an elliptic body[13]. The participants in the Key Task 2-19 study included the: Defence Science and Technology Laboratory (Dstl), UK; National Research Council (NRA), Canada; Air Force Research Laboratory (AFRL), US; Army Research Laboratory (ARL), US; and NASA Langley Research Center (LaRC), US.

The purpose of this paper is to present the results of a wind-tunnel investigation, which provided the experimental data for comparing with the various CFD codes used by the participants of the Key Task 2-19 study, of non-axisymmetric missile configurations. The missile configurations consisted of a square cross-section body with tail fins that could be mounted on the body corners or on the body sides. Surface pressures, vapor screen, and force data were obtained over an angle of attack range of -4° to 24° at Mach numbers of 2.50 and 4.50. These wind-tunnel tests were conducted in the NASA Langley Unitary Plan Wind Tunnel (UPWT).

II. Apparatus and Experimental Methods

A. Wind Tunnel

The wind-tunnel test was conducted in the UPWT which is a continuous- flow, variable-pressure supersonic wind tunnel. The tunnel contains two test sections, which are approximately 4 ft square and 7 ft long. Each test section covers only part of the Mach number range of the tunnel. The nozzle ahead of each test section consists of an asymmetric sliding block, which allows continuous Mach number variation during tunnel operations from 1.5 to 2.9 in the low Mach number test section (#1) and 2.3 to 4.6 in the high Mach number test section (#2). A complete description of the facility along with test section calibration information is contained in Ref. 14.

This test was conducted in test section #2 at the average free-stream conditions shown in Table 1.

Table 1: Wind tunnel test conditions.

M	$Re \times 10^{-6}$, per ft	p_o, psfa	T_0, deg F	q, psfa	p, psfa
2.50	4.0	3239	130	829	190
4.50	4.0	9332	150	457	32.2

The tunnel air dew point was maintained at sufficient levels to minimize water vapor condensation effects during all phases of the test except the vapor screen portion of the test.

B. Model Description

The square cross-section missile model was provided by the Dstl as part of the collaborative effort. This configuration was chosen as the test article because it could easily be adapted from an existing non-axisymmetric model with only minor modifications. These included a new forebody, side mounted tail fins, corner mounted tail fins, and surface pressure orifices. In addition, the configuration was comparable with an existing circular cross-section missile design for which a large experimental database is available[1]. A sketch of the square cross-section body alone is presented in Fig. 1. The model was composed of a circular arc nose and a separate square cross-section body. The model roll angle was defined as 0° when the missile body viewed from the aft end looking upstream was diamond shaped. A photograph of the model with side mounted tail fins at a roll angle of 0° is shown in Fig. 2.

Both the side and corner mounted tail fins were attached to the body at the same longitudinal hinge line location (x/D=11.5) as indicated in Fig. 1. Sketches of the side and corner mounted tail fins are shown in Fig. 3. The corner mounted fins were designed by rotating the side mounted fins about the missile longitudinal center line by 45 deg and only keeping the portion of the fin that would remain outside of the missile body. The span of both sets of fins was 11.10 in. The side mounted tail fins had the capability to deflect to ±10 deg in 5 deg increments. A limited amount of data were acquired with the side fins deflected, however, these data will not be presented in this paper.

A total of 180 surface pressure orifices were installed on the model at three longitudinal model stations (MS) as shown in Fig. 1. Each model station contained 60 surface pressure orifices with 15 orifices on each side of the model. The orifices were arranged symmetrically about the centerline of each model face.

C. Boundary Layer Transition Strips

The model was tested with boundary layer transition strips on the model nose and on the tails. The transition strip on the model nose consisted of #35 (0.0216 in. average size) sand-grit individually spaced 0.086 in. apart and located 1.8 in. from the model nose measured along the model surface. The transitions strips on the fins consisted of #40 (0.0181 in. average size) sand-grit individually spaced 0.102 in. apart and located 0.60 in. from the fin leading edge measured streamwise. The sizing and location of the transition strips were determined using the methods and data from Refs. 15 and 16 except that a critical roughness Reynolds number of 1800 was used instead of the recommended 600. The increased critical roughness Reynolds number was used to properly account for the effect of Mach number.

D. Measurements and Corrections

1. Force and moment data

Force and moment data were obtained with a 6-component electrical strain gage balance which had three platinum resistance thermometers located on the forward, middle, and aft sections of the balance. The balance temperature was estimated from the average of the three platinum resistance thermometers and was used to correct the balance sensitivities for temperature. The estimated uncertainties of the balance measurements based on the balance calibration are shown in Table 2.

Table 2: Estimated balance uncertainty values.

Longitudinal component	Estimated uncertainty	Lateral component	Estimated uncertainty
NF	0.5 lb	RM	1.1 in-lb

Table 2: Estimated balance uncertainty values. (Continued)

Longitudinal component	Estimated uncertainty	Lateral component	Estimated uncertainty
AF	0.2 lb	YM	1.1 in-lb
PM	1.3 in-lb	SF	0.7 lb

The balance moment reference center was located at model station 27.75. As shown in Fig. 4, the final force and moment data are referred to an axis system that was located at the model nose and was oriented such that the model normal force remained in a fixed vertical plane regardless of the model roll angle. All of the data have been reduced using a reference area based on a circular cross-section with a diameter equal to the length of the square body side rather than the square body cross sectional area. This reference area was chosen so that the data could be directly compared with the wind tunnel data which used a circular cross-section missile[1].

The axial force data were corrected to the condition of free stream static pressure acting over the model base and chamber areas. Chamber pressure was measured using two pressure tubes located near the model balance. The chamber pressures were measured with individual 5 psia strain gage transducers and were averaged before being used to correct the axial force data. The model base pressure was measured at four locations around the base using individual pressure tubes connected to 5 psia strain gage transducers. The base pressure tubes were only installed for the force and moment portion of the test. The base pressure tubes were originally bent in an “L” shape such that the end of the tubes were approximately 0.15 in. from the model base and located approximately three quarters of the distance between the model center line and the model corners. However, during the initial force and moment runs it was discovered that the model was deflecting on the balance and sting to such an extent at certain model attitudes at M=2.50 that some of the base pressure tubes were exposed to the flow outside the base region. In order to correct this condition, the tubes were connected to short lengths (approx. 5 in.) of flexible tubing and the ends were glued to the model base with an epoxy adhesive for the remainder of the force and moment runs. For the data points that had “L” shaped base pressure tubes exposed to flow outside of the base region, the three base pressure tubes that remained in the base flow region were averaged before being used in the data reduction; for all other test conditions, the four base pressures were averaged. A photograph of the base pressure tubes is shown in Fig. 5.

The model angle of attack has been corrected for both tunnel flow angularity and for sting and balance deflections caused by aerodynamic loads. During the force and moment portion of the test, flow angularity was determined from the balance force measurements by determining the pitch angle at which the model normal force was zero. Because the flow angularity value determined from the balance data was an average flow angularity over the entire model, this flow angularity was used in the final data reduction of all the data.

2. Surface pressures

The surface pressures were measured with four 48-port, 10-psid electronically scanned pressure (ESP) modules which were operated as absolute gages and located outside of the tunnel. Short lengths of flexible tubing ran from the model orifices through tee-shaped channels machined in the corners of the model to the rear of the model. At this point, the flexible tubing connected to approximately 12 ft of 0.060 in. diameter stainless steel tubing, which was routed through the side of the tunnel to the ESP modules. In addition to the model surface pressures connected to the ESP modules, three check pressures were connected to the last three ports on each module for use as a system check to ensure that the module was working properly. These check pressures were set to approximately 100 psfa, 300 psfa, and 700 psfa and were independently measured with three bourdon-tube pressure gages. The uncertainty of the pressure measurements using the ESP modules is estimated to be ±1.5 psfa.

Surface pressures were only obtained for the body alone configuration. During the surface pressure measurement portion of the test, flow angularity was estimated from the pressure difference between two orifices located on the top and bottom of the model nose. The flow angularity values estimated during the pressure portion of the test were only used for online data acquisition of the surface pressure data. The final flow angularity values were determined from force and moment measurements as discussed previously.

3. Tunnel conditions

The tunnel stagnation pressure was measured with a 150 psia bourdon-tube pressure transducer, which has an estimated uncertainty of ±1 psfa. The tunnel stagnation temperature was measured with a platinum resistance thermometer, which has an estimated uncertainty of ±0.75 °F.

E. Vapor Screen Test Technique

The vapor screen test technique was used to visualize the off-body flow field of the missile. The vapor screen technique basically consists of injecting water into the tunnel circuit until a fog is formed in the test section. The fog is a result of the water vapor condensing as the static temperature of the air decreases in the expanding flow of the tunnel nozzle. A thin light sheet is passed across the test section illuminating the fog. Photographs of the fog and light sheet are recorded with both still and video cameras located inside the test section. The light sheet remains stationary while the model is traversed longitudinally through the light sheet. A schematic of the vapor screen experimental setup is shown in Fig. 6; additional details of the vapor screen technique can be found in Ref. 17.

For this particular test, an argon laser was used as the light source to illuminate the fog. A fiber optic cable was used to connect the laser with the optics package which transformed the laser from a conical beam as it exited the fiber optic cable to a 0.25 in. thick sheet. The model was painted black (regular flat black spray paint) to reduce reflections of the laser light sheet. White dots were painted on the body as shown in Fig. 7 to provide a visual indication of the position of the model relative to the light sheet during tunnel operations. Still photographs were only obtained at positions 4, 7, 9, and 11. The model surface pressure orifices were located at positions 4, 7, and 10. Still photographs were not obtained at position 10 because the missile fins would be blocking much of the laser light sheet at that position. As shown in Fig. 8, a video camera was mounted outside the tunnel on the access door so that the white dots could be viewed to position the model in the light sheet.

Figure 9 shows a view inside the test section of the model, still camera housing, and video camera housing. The still camera housing was mounted approximately 12 in. from the tunnel ceiling and approximately 4 in. to the right of the model pitch plane, i.e., on the side of the model opposite of the laser light source. Unfortunately, the view from the still camera of the left-hand side of the model, which was illuminated by the laser light sheet, was partially obscured by the model. However, a small video camera was mounted on the left-hand side of the model support system approximately 2 ft from the end of the model and recorded real-time images of the vapor screen as the model was moved through the light sheet. The video images provided additional information on the existence and location of the model vortices and were invaluable in analyzing the data from this investigation.

The still camera used regular film, which was processed after the vapor screen runs were completed. The film negatives were then electronically scanned.

Vapor screen photographs were obtained at angles of attack of 8°, 14°, and 20° and model roll angles of -22.5°, 0°, 22.5°, and 45° for the body with tail fins mounted on the side and corner of the model. Video graphic data were obtained while both longitudinally translating the model and rolling the model. No vapor screen data were obtained with deflected side mounted fins.

III. Results and Discussion

Table 3 shows the primary CFD test cases for the TTCP study.

Table 3: CFD test cases for square cross-section missile.

Fin location	M	α	ϕ
Corner	2.50	14°	0°, 22.5°, 45°
	4.50		
Side	2.50	14°	0°, 22.5°, 45°
	4.50		
Corner	2.50	24°	0°

Since the majority of test cases were at $\alpha = 14°$, the results presented in this paper will concentrate on the $\alpha = 14°$ test cases. However, all of the test data were provided to the Key Task 2-19 study participants.

A. Surface Pressure Results

Figure 10 presents the surface pressure distributions for the body alone at $\alpha = 14°$ for roll angles of 0°, 22.5°, and 45° at Mach numbers of 2.50 and 4.50. The abscissa on each plot is the angular location (θ) of the pressures measured

clockwise from the 12 o'clock position as shown in the diagram in Fig. 10. The location of $\theta = 0°$ remains fixed as the model is rolled.

Because the configurations with $\phi = 0°$ (diamond) and 45° (square) are symmetric and data were obtained at a moderate angle of attack, it would be expected that the pressure distributions should also be symmetric. Inspection of the Fig. 10. confirms that the pressure distributions are symmetric and this symmetry also indicates the good fidelity of the pressure measurements. In addition, it would be expected that the sharp-edge separation (Ref. 18) at the corners of the model would create large pressure gradients and would be a major feature of the pressure distributions. Again, inspection of the data show this to be the case especially for the M = 2.50 data.

For both M = 2.50 and 4.50, the pressure distributions on the windward side of the body remain virtually unchanged at the three model stations down the length of the body. However, the flow field on the leeward side of the model contains vortices and flow separation, which affect the pressure distributions down the length of the body. The pressure gradients on the leeward faces are generally smaller at M = 4.50 than at M = 2.50.

An example of vortices affecting the leeward model face pressure distribution can be seen in the $\phi = 0°$ (diamond) configuration at M = 2.50. At x/D= 5.5, the data show a low pressure region near $\theta = 50°$ and 310° just past the model corners indicating the presence of the lee side vortices. At x/D = 8.5, this low pressure region has moved near $\theta = 40°$ and 320° and by x/D = 11.5 the low pressure region has essentially disappeared indicating that the vortices have moved away from the body and do not influence the surface pressures. At M = 2.50 for the $\phi = 22.5°$ (asymmetric) configuration, it is interesting to note that the pressure distributions on the leeward faces ($292.5° < \theta < 360°$ and $0° < \theta < 112.5°$) do not change significantly from x/D = 8.5 to 11.5. Evidently, the lee-side vortices are far enough away from the body at x/D = 8.5 so that they do not significantly influence the surface pressures.

B. Force and Moment Results

1. Effect of model roll angle

Force and moment results as a function of angle of attack for the body alone are presented in Fig. 11. Both longitudinal and lateral results are presented for Mach numbers of 2.50 and 4.50. The longitudinal data show that the body alone at 0° roll (diamond) has the largest normal force followed by the $\phi = 22.5°$ (asymmetric) and $\phi = 45°$ (square) configurations. Balance limits prevented data from being acquired up to 24° at M = 2.50. Axial force remained fairly constant across the angle of attack range at M = 2.50. At M = 4.50, axial force remained fairly constant up to approximately $\alpha = 15°$ then increased at a faster rate. The most significant differences between the M=2.50 and 4.50 data were in the lateral force and moment data. For the two symmetric configurations ($\phi = 0°$ and 45°), the lateral coefficients were essentially zero as expected. However, the $\phi = 22.5°$ configuration showed large yawing-moment and side-force coefficients which peaked near the maximum angle of attack range for the M = 2.50 case. In contrast, at M= 4.50, the yawing-moment and side-force coefficients peaked at approximately $\alpha = 14°$ and decreased to near zero at $\alpha = 24°$. The rolling-moment coefficient on the body alone was consistent at M = 2.50 and 4.50. The reason for this behavior is not understood at this time.

Force and moment results for the body with fins located on the corner and side are shown in Fig. 11b and 11c, respectively. The basic trends discussed for the body alone case also apply to these data except for the rolling-moment data. The rolling-moment data for the body with corner-mounted fins shows a roll reversal at approximately 12° angle of attack at M = 2.50. The body with side-mounted fins has a larger peak negative rolling-moment compared to the corner-mounted fins and the roll reversal occurs near $\alpha = 17°$. The rolling-moment trends are similar at M = 4.50 although the magnitude of the peak negative rolling-moment is much less and the roll reversal occurs at lower angles of attack. This roll reversal phenomenon is probably the result of interaction between the body vortices and the tail fins.

2. Configuration comparisons

Shown in Fig. 12 are force and moment coefficient comparisons as a function of angle of attack for the body alone and body with fins for model roll angles of 0°, 22.5°, and 45°. At all roll angles, the longitudinal data show that the addition of fins slightly increases the normal force compared to the body alone, however, there is little difference between the normal force for the corner and side mounted tail fin configurations. Similar results occurred with pitching moment where the addition of fins resulted in a decrease in the measured pitching moment. The addition of fins also increases axial force with the side mounted fins having a larger axial force than the corner mounted fins. This result is mainly caused by the larger exposed fin surface area of the side mounted fin.

The lateral force and moment data for roll angles of 0° and 45° (Figs. 12a and 12c) show essentially no load because the configurations are symmetric about a vertical plane. However, at $\phi = 22.5°$ (Fig. 12b), the yawing-moment and side force data for the body with either side- or corner-mounted fins show a cross over with the body alone data, which occur over the angle of attack range of approximately 12° to 18° at M = 2.50. The same trend is visible in the side force data although the effect is smaller. The rolling-moment data show that the body with corner fins have a roll reversal at an angle of attack near 12° while roll reversal for the body with side fins occurs near $\alpha = 17°$. These effects are probably caused by the asymmetric sharp edge body vortices interacting with the tails.

C. Vapor Screen Results

In order to orient the reader to the vapor screen images to be presented, Fig. 13 shows a sample vapor screen image with some of the more prominent features identified. The image view is from above and behind the model looking upstream as discussed previously in Fig. 9. The light sheet illumination source is located to the left of the image and shines to the right creating a shadow of the missile body. The light sheet is actually a wedge shape across the test section. The model support hardware can been seen in this image, however, in some images the hardware will be out of view because the model has been moved downstream so that the flow field near the nose can be viewed. In some cases, the model nose shock will not be visible because it has grown large enough to be out of the camera field of view.

Vapor screen photographs of the body at $\alpha = 14°$ for roll angles of 0°, 22.5°, and 45° at Mach numbers of 2.50 and 4.50 are shown in Fig. 14 for the corner mounted fins and Fig. 15 for the side mounted fins. In order to present images of reasonable size, only images at x/D = 10.5 and 12.5 are shown in Figs. 14 and 15. The images at x/D = 10.5 should be essentially identical between the two configurations at the same Mach number because this station was located forward of the fins.

All of the vapor screen photographs show two vortex formations that have formed as the flow separates from the sharp corners of the model. As expected, the vortex formations are symmetric for the $\phi = 0°$ and 45° cases. At M = 2.50, the vortices are essentially circular as compared to the vortices at M = 4.50, which have elongated and are generally located further from the body. The images at x/D = 12.5, which is aft of the fins, show that the fins do not have a major affect on the shape or position of the vortices. The primary difference between the images before and after the fins is the addition of shock waves from the fins.

For the $\phi = 22.5°$ case, the vortex that has formed from the flow separation around the upper left hand corner is positioned above the left hand leeward facing side along the length of the body. In contrast, the vortex formed from the flow separation around the upper right hand corner remains positioned on top of the corner along the length of the body. Again, the fins do not appear to significantly affect the shape or position of the vortices.

IV. Conclusions

A wind tunnel investigation has been conducted to acquire surface pressure, vapor screen, and force and moment data on a slender square cross-section missile body at Mach numbers of 2.50 and 4.50 for comparison with computational fluid dynamics (CFD) results from various computer codes. The missile body was tested with tail fins mounted on the body corners as well as the body sides over a roll angle range of 0° (diamond shape) to 45° (square shape). Although a significant amount of data were acquired during this test, a limited data set that primarily corresponded to the CFD test cases was presented in this paper. The significant conclusions from the limited test data were:

1. Vortex formation from the sharp-edge flow separation about the body corners was a significant contributor to the overall missile flow field.
2. The addition of tail fins resulted in a slight increase in the missile normal force over the body alone.
3. The location of the tail fins (corner or side mounted) did not significantly affect the missile normal force.
4. At model roll angles of 22.5° (asymmetric orientation) and at M = 2.50, the side-force and yawing-moment continuously increased as angle of attack increased to 24°. However, at M = 4.50, the side-force and yawing-moment increased to a maximum near $\alpha = 14°$ the decreased to near zero at $\alpha = 24°$.
5. The missile tail fins did not appear to significantly affect the shape or position of the vortices.

Acknowledgments

The UK element of this work was carried out as part of the Weapon and Platform Effectors Domain of the Ministry of Defence (MoD) Research Programme.

References

[1]Birch, T. J.; Allen, J. M.; and Wilcox, F. J.: Force, Surface Pressure and Flowfield Measurements on a Slender Missile Configuration at Supersonic Speeds. AIAA Paper 2000-4207, 2000.

[2]Bulbeck, C. J.; Morgan, J.; and Fairlie, B. D.: RANS Computations of High-incidence Missile Flow Using Hybrid Meshes. AIAA Paper 2000-4209, 2000.

[3]Sahu, Jubaraj; and Heavey, Karen R.: Application of CFD to High Angle of Attack Missile Flowfields. AIAA Paper 2000-4210, 2000.

[4]Birch, T. J.; Wrisdale, I. E.; and Prince, S. A.: CFD Predictions of Missile Flowfields. AIAA Paper 2000- 4211, 2000.

[5]Lesage, F.; Nicolle, J.; and Boulianne, M. A.: Navier-Stokes Computations of High Angle of Attack Missile Flowfields. AIAA Paper 2000-4212, 2000.

[6]Sturek, Walter B., Sr.; and Taylor, Malcolm S.: Statistical Analysis of CFD Results for Missile Surface Pressures. AIAA Paper 2000-4214, 2000.

[7]Burnley, V.; Hoke, C.; and Schwabacher, G: Aerodynamic Analysis of Complex Missile Configurations Using AVUS (Air Vehicles Unstructured Flow Solver). AIAA Paper 2004-5452, 2004.

[8]Birch, T., and Petterson, K.: CFD Predictions of Square and Elliptic Cross-section Missile Configurations. AIAA Paper 2004-5453, 2004.

[9]Trickey, C.; Edwards, J.; Faminu, O.; Hathaway, W.; and Shaw, S.: Experimental and Computational Assessment of the Dynamic Stability of a Supersonic Square Section Missile. AIAA Paper 2004-5454, 2004.

[10]Mcllwain, S.; and Khalid, M.: Computations of Square and Elliptical Section Missiles Using WIND. AIAA Paper 2004-5455, 2004.

[11]Sahu, J.; Silton, S.; and Heavey, K.: Numerical Computations of Supersonic Flow over Non-Axisymmetric Missile Configurations. AIAA Paper 2004-5456, 2004.

[12]Edwards, J.: Evaluation of Computational Methods with Experiment for Non-circular Missile Configurations – An Overview. AIAA Paper 2004-5457, 2004.

[13]Allen, Jerry M: Force, Surface Pressure, and Flowfield Measurements on an Elliptical Body Concept at Supersonic Speeds. AIAA Paper 2004-5450, 2004.

[14]Jackson, Charlie M., Jr.; Corlett, William A.; and Monta, William J.: Description and Calibration of the Langley Unitary Plan Wind Tunnel. NASA TP-1905, 1981.

[15]Braslow, Albert L.; Hicks, Raymond M.; and Harris, Roy V., Jr.: Use of Grit-Type Boundary-Layer-Transition Trips on Wind Tunnel Models. NASA TND-3579, Sept. 1966.

[16]Braslow, Albert L.; and Knox, Eugene C.: Simplified Method for Determination of Critical Height of Distributed Roughness Particles for Boundary Layer Transition at Mach Numbers from 0 to 5. NACA TN 4363, Sept. 1958

[17]Morris, Odell A.; Corlett, William A.; Wassum, Donald L.; and Babb, C. Donald: Vapor-Screen Technique for Flow Visualization in the Langley Unitary Plan Wind Tunnel. NASA TM 86384, July 1985.

[18]Wood, Richard M.; Wilcox, Floyd J., Jr.; Bauer, Steven X. S.; and Allen, Jerry M.: Vortex Flows at Supersonic Speeds. NASA/TP-2003-211950, March 2003.

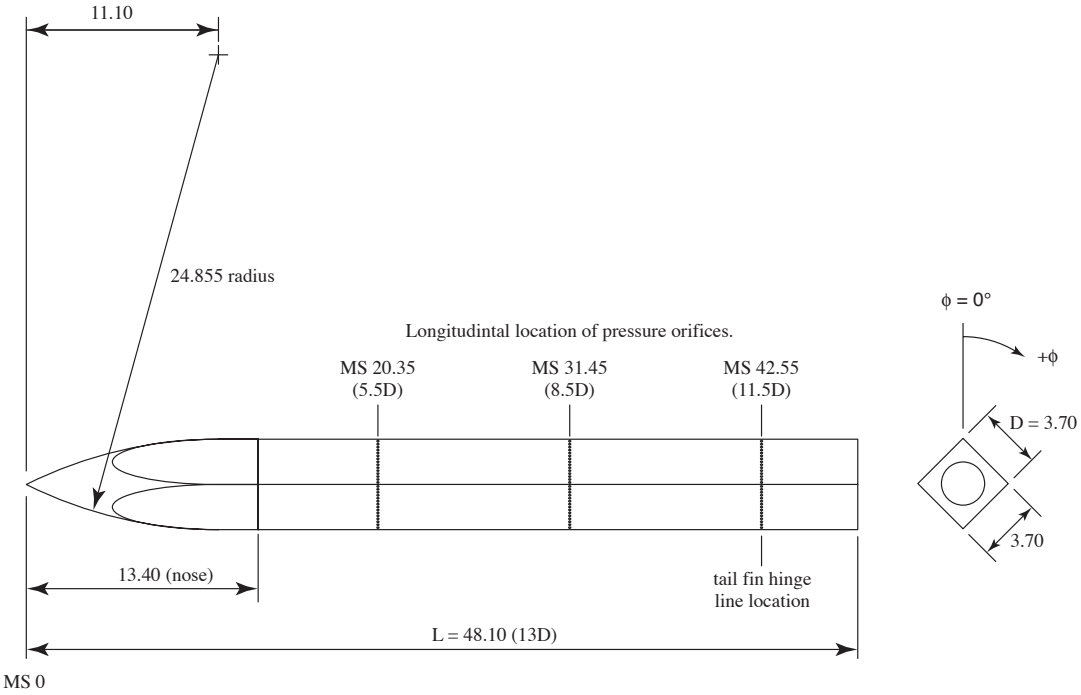

Figure 1. Body alone sketch. Dimensions are in inches unless otherwise noted.

Figure 2. Photograph of model with side mounted tail fins at 0° roll mounted in the Langley UPWT.

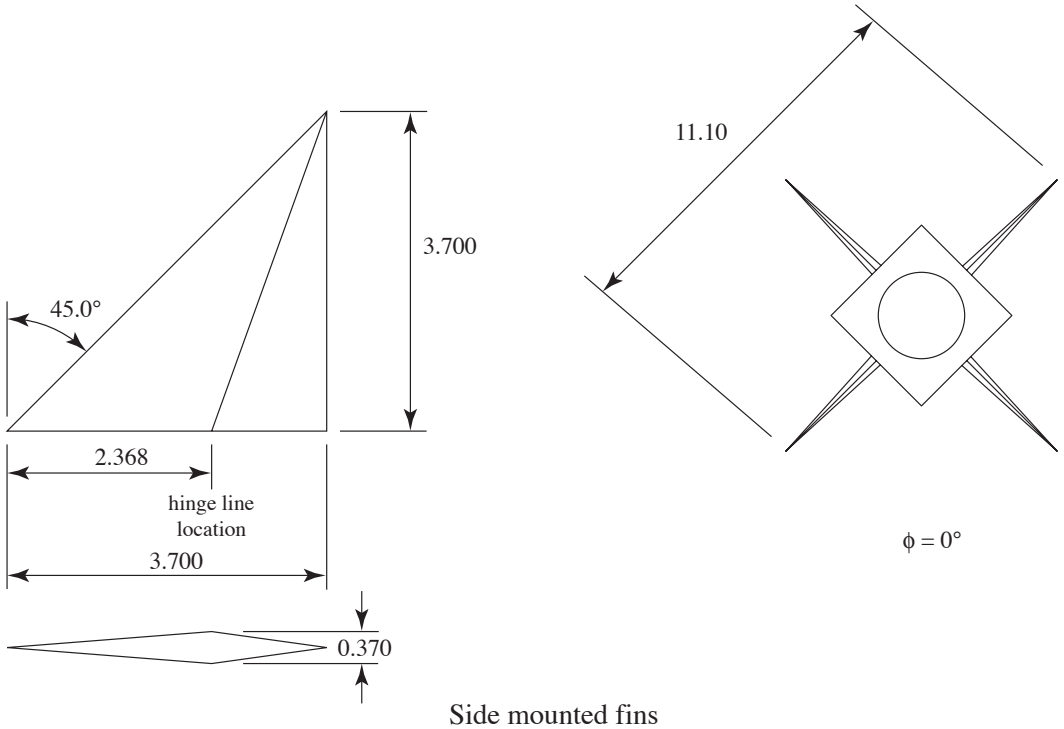

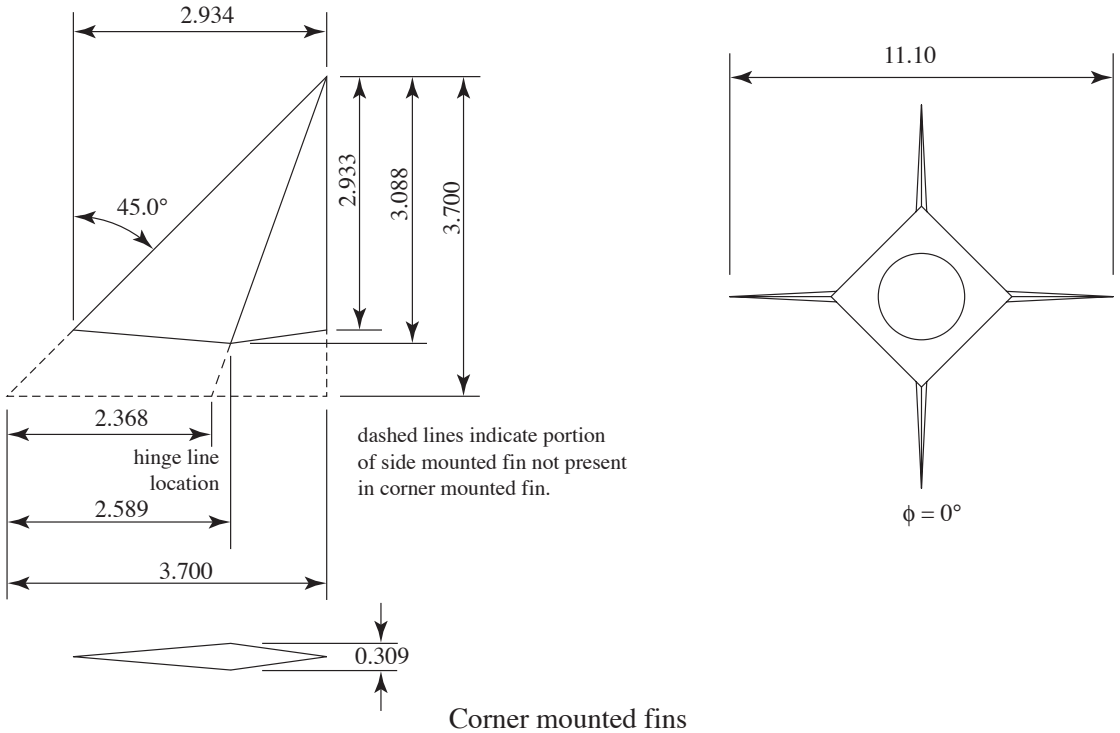

Figure 3. Sketch of side and corner mounted tail fins. All dimensions are in inches unless otherwise noted.

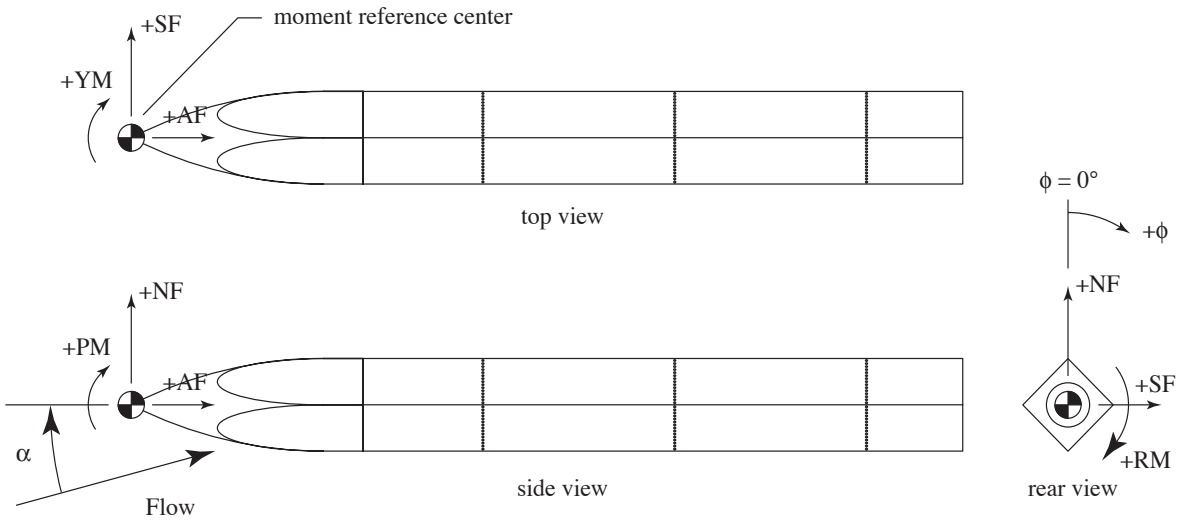

reference area (A) = 0.074667 sq ft
reference length (D) = 3.70 in.

Note: NF always lies in pitch plane (α plane) regardless of model roll angle (ϕ).

Figure 4. Location of model moment reference center.

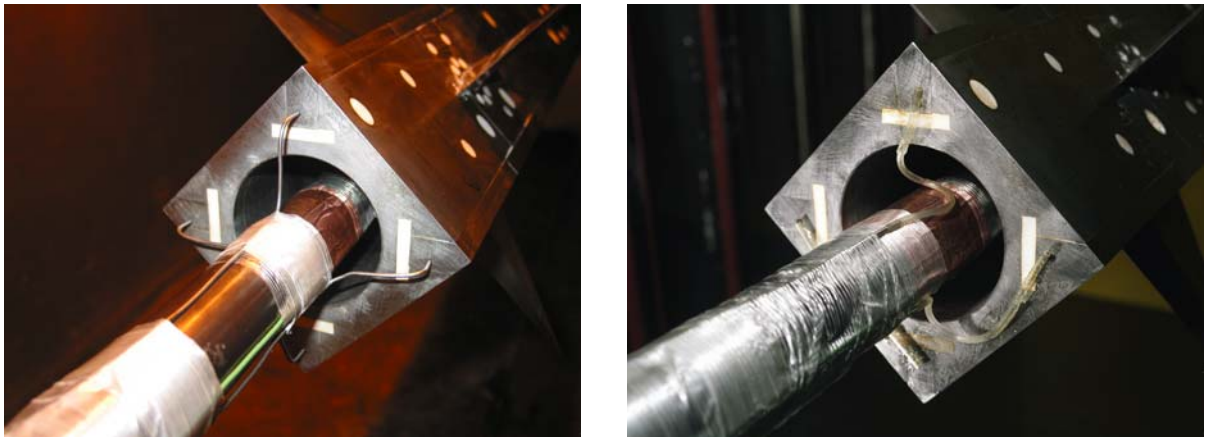

a. "L" shaped tubes. **b. Flexible tubes.**

Figure 5. Photograph of base pressure tubes.

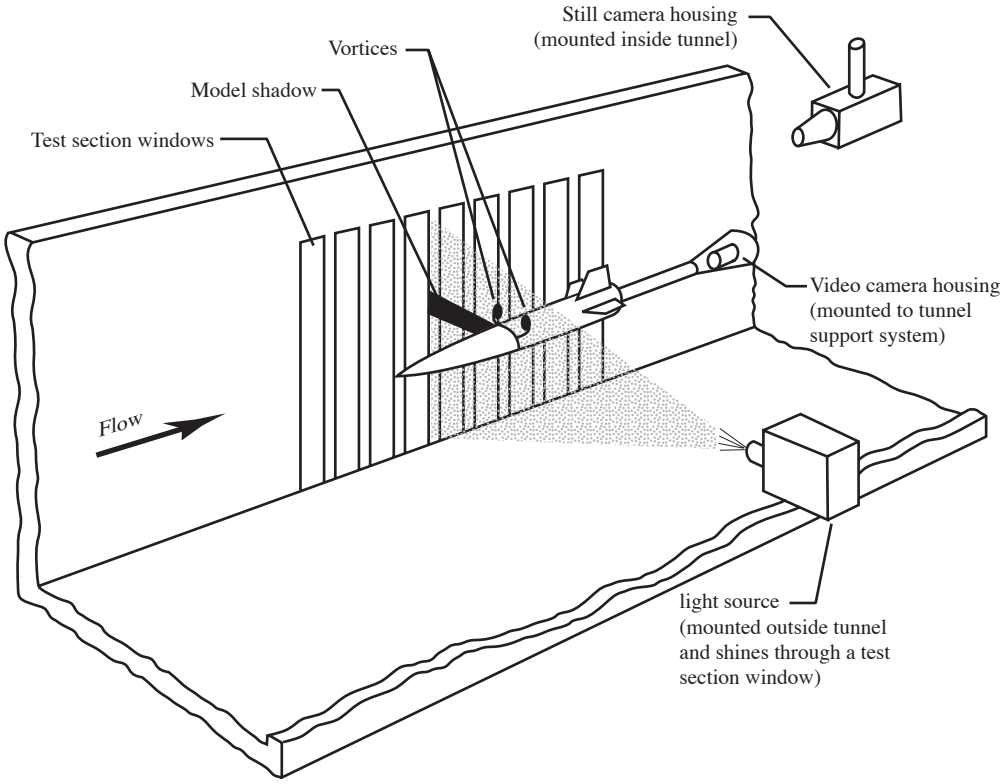

Figure 6. Vapor screen experimental set up.

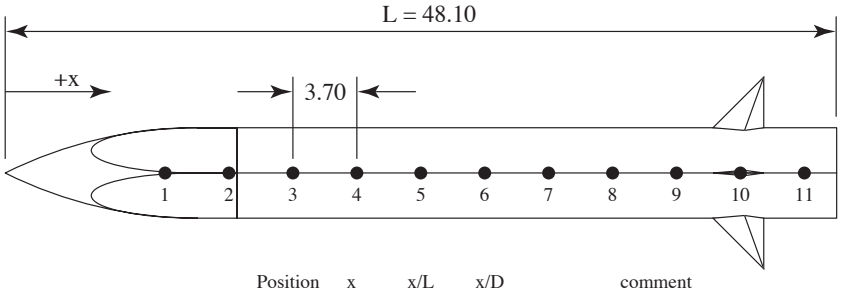

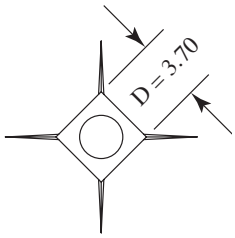

	Position	x	x/L	x/D	comment
	1	9.25	0.192	2.5	
	2	12.95	0.269	3.5	
	3	16.65	0.346	4.5	
still photograph ⇒	4	20.35	0.423	5.5	location of surface pressure orifices
	5	24.05	0.500	6.5	
	6	27.75	0.577	7.5	
still photograph ⇒	7	31.45	0.654	8.5	location of surface pressure orifices
	8	35.15	0.731	9.5	
still photograph ⇒	9	38.85	0.808	10.5	
	10	42.55	0.885	11.5	location of surface pressure orifices
still photograph ⇒	11	46.25	0.962	12.5	

Figure 7. Sketch of vapor screen positioning dots. All dimensions are in inches unless otherwise noted.

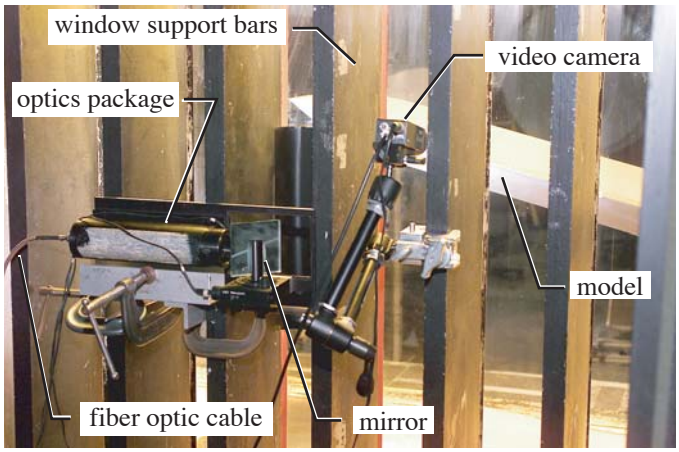

Figure 8. View of vapor screen optics package and video camera installation on test section window.

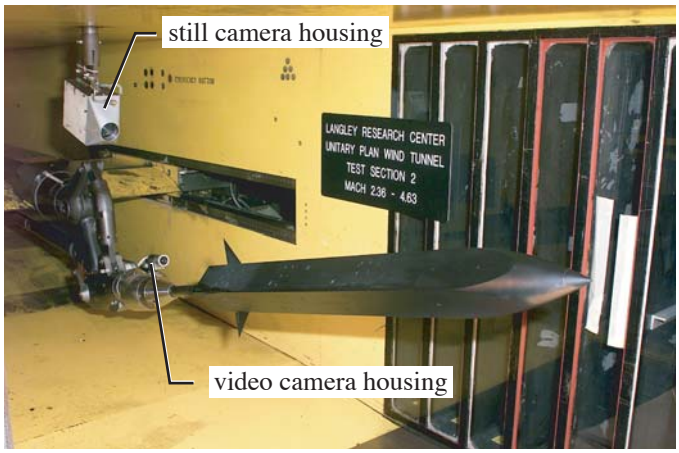

Figure 9. View of still and video camera housings used to record vapor screen images.

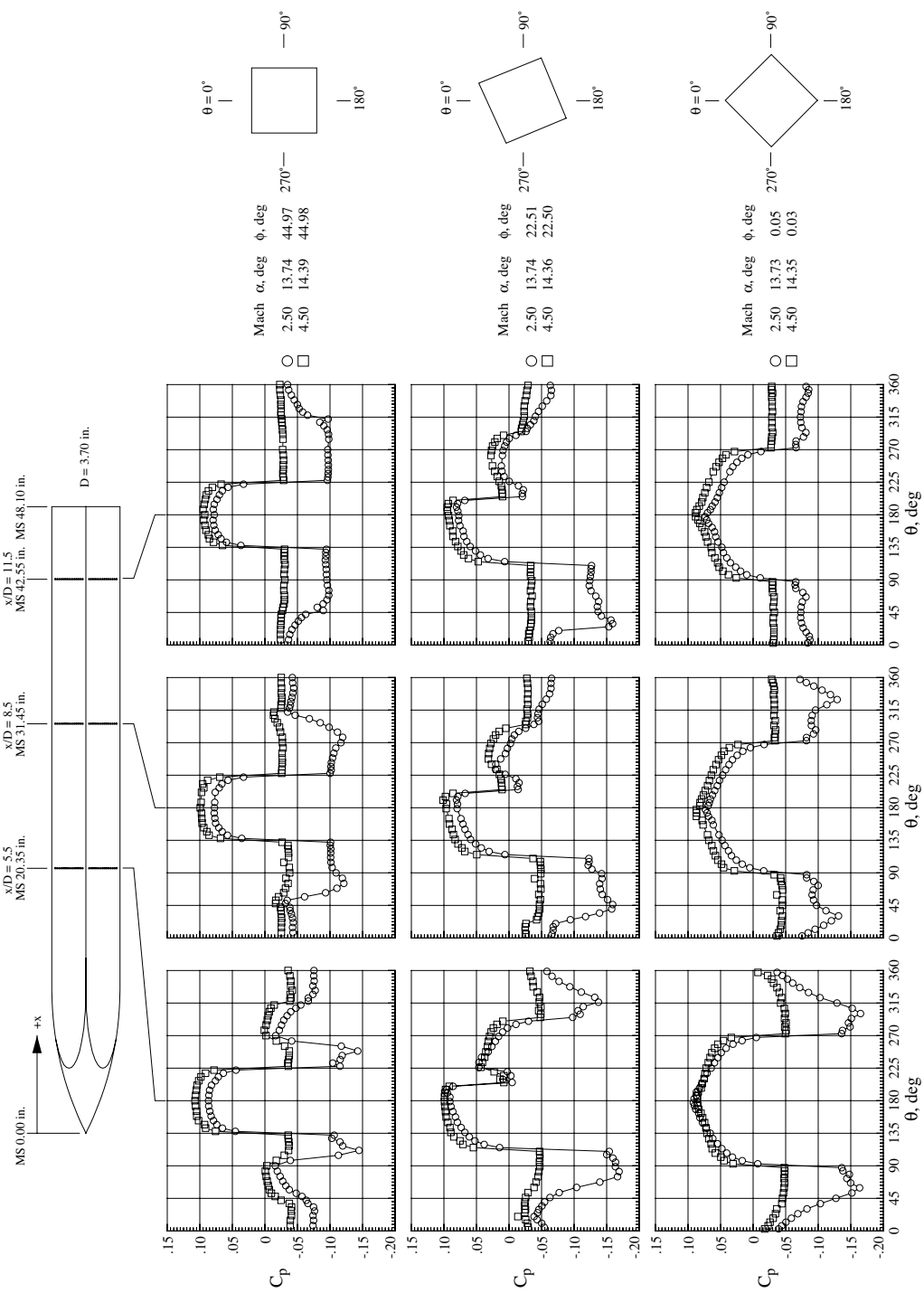

Figure 10. Body alone surface pressure distributions.

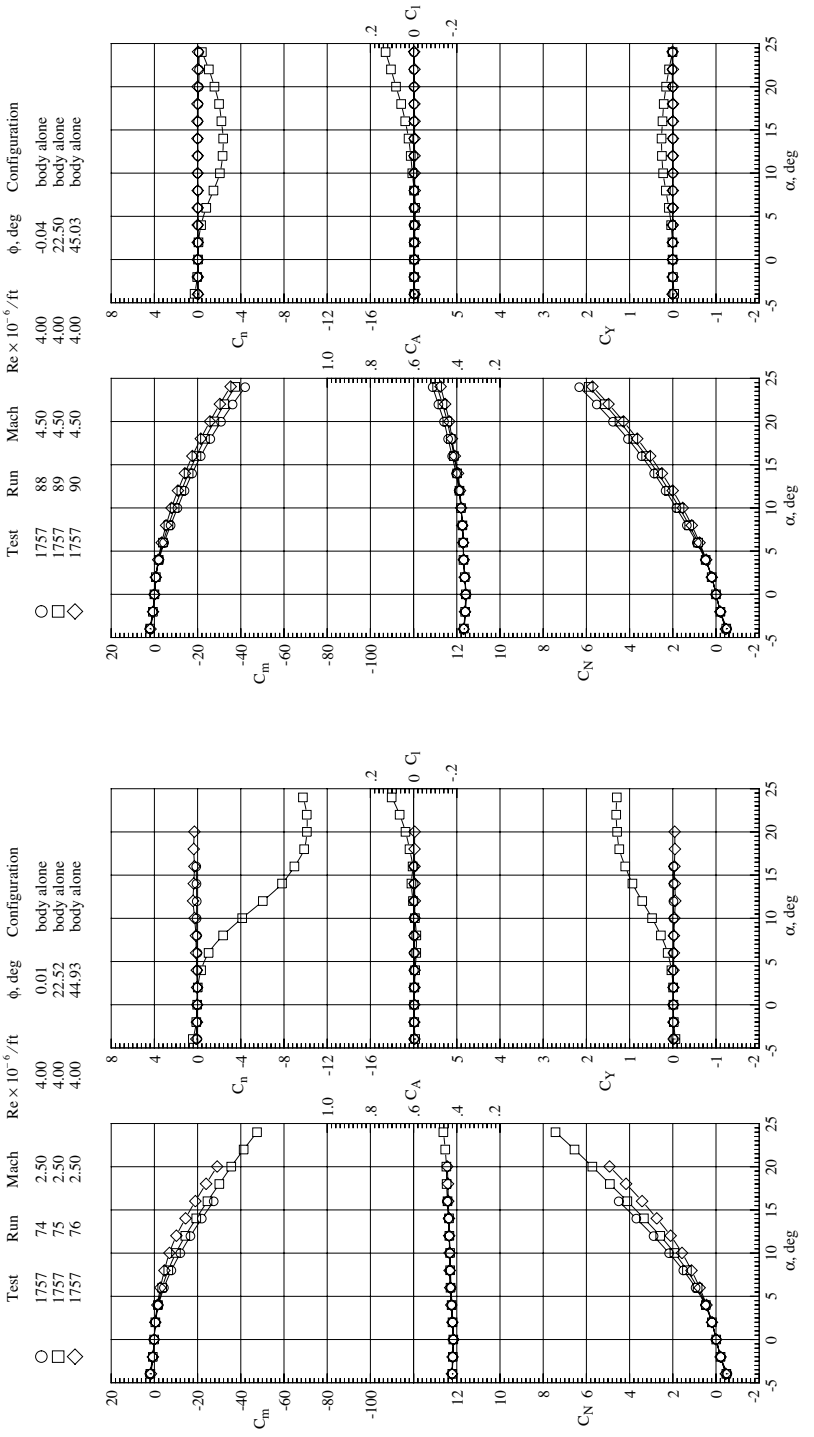

a. Body alone.

Figure 11. Force and moment comparisons at roll angles of 0°, 22.5°, and 45°.

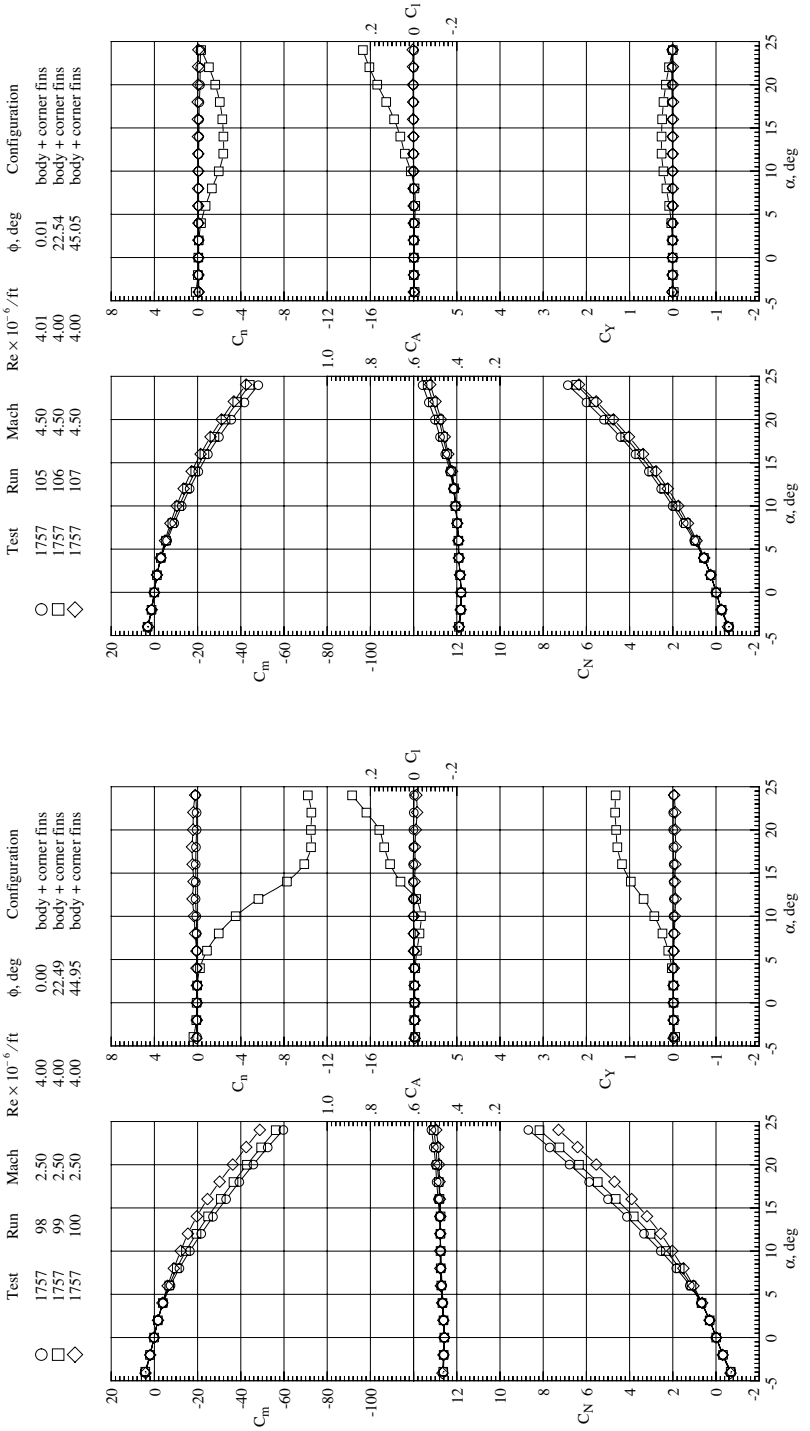

b. Body with corner mounted tail fins.
Figure 11. Continued.

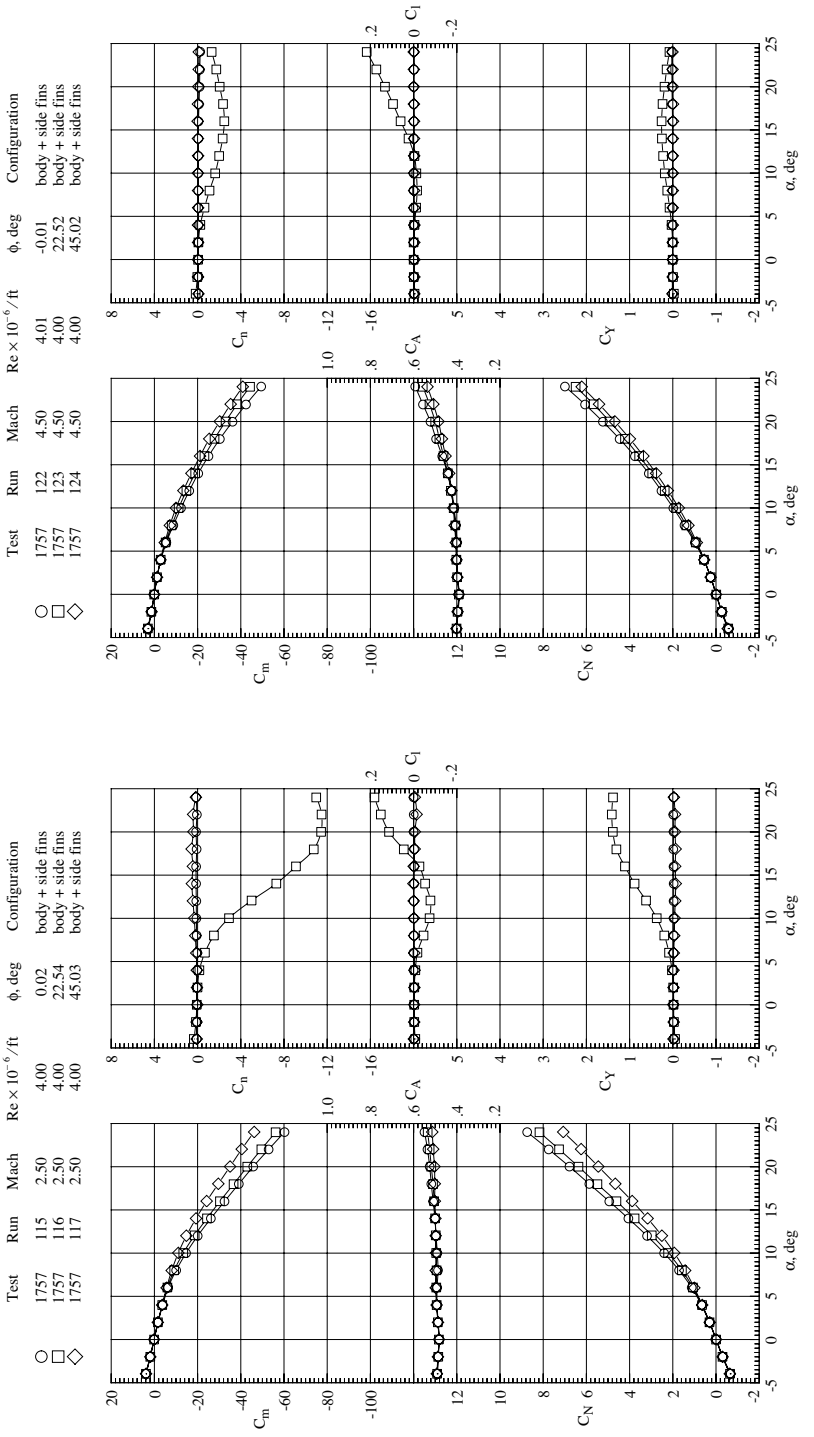

c. Body with side mounted tail fins.
Figure 11. Concluded.

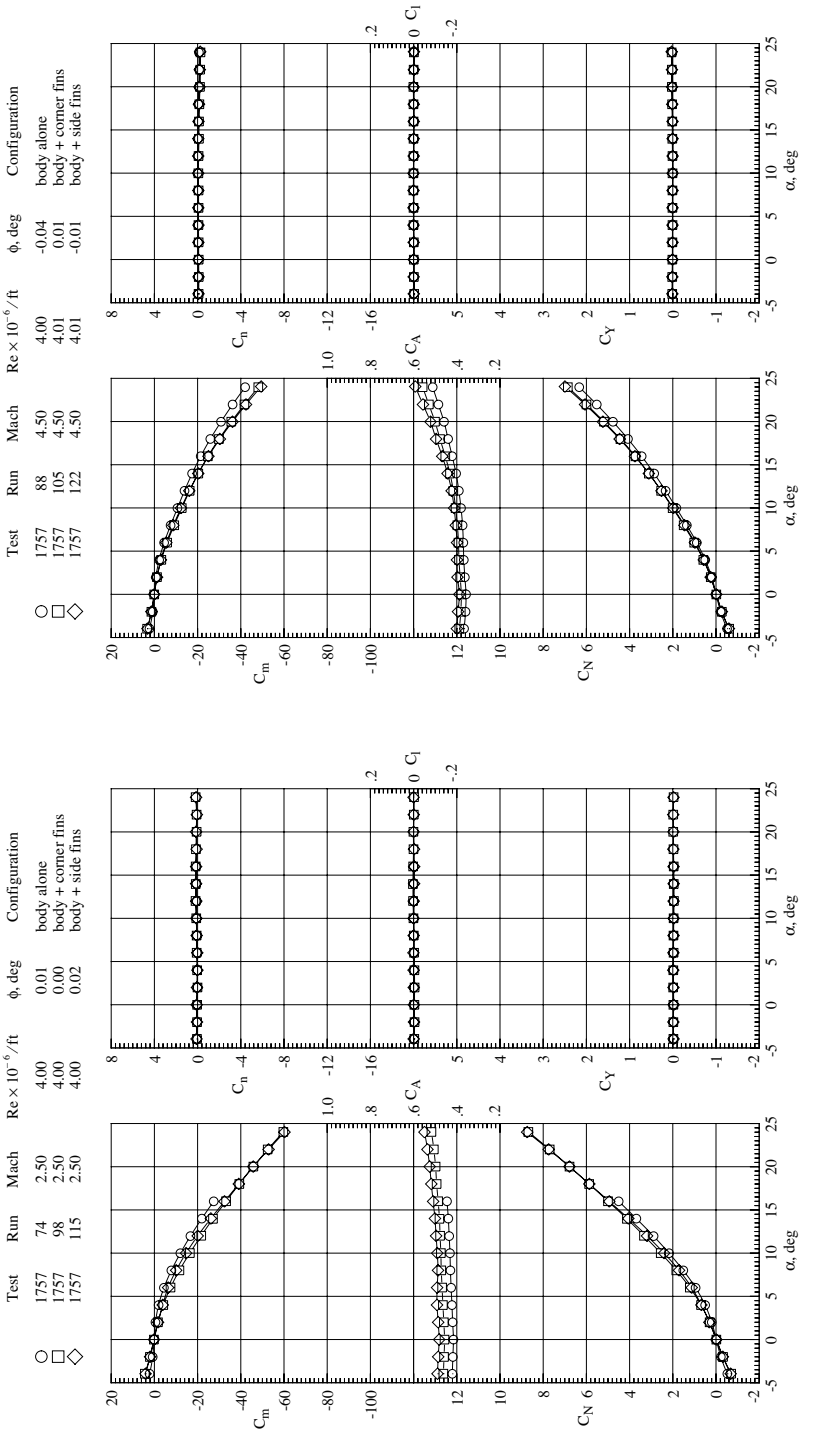

a. 0° roll.

Figure 12. Force and moment comparisons between body and body with fins.

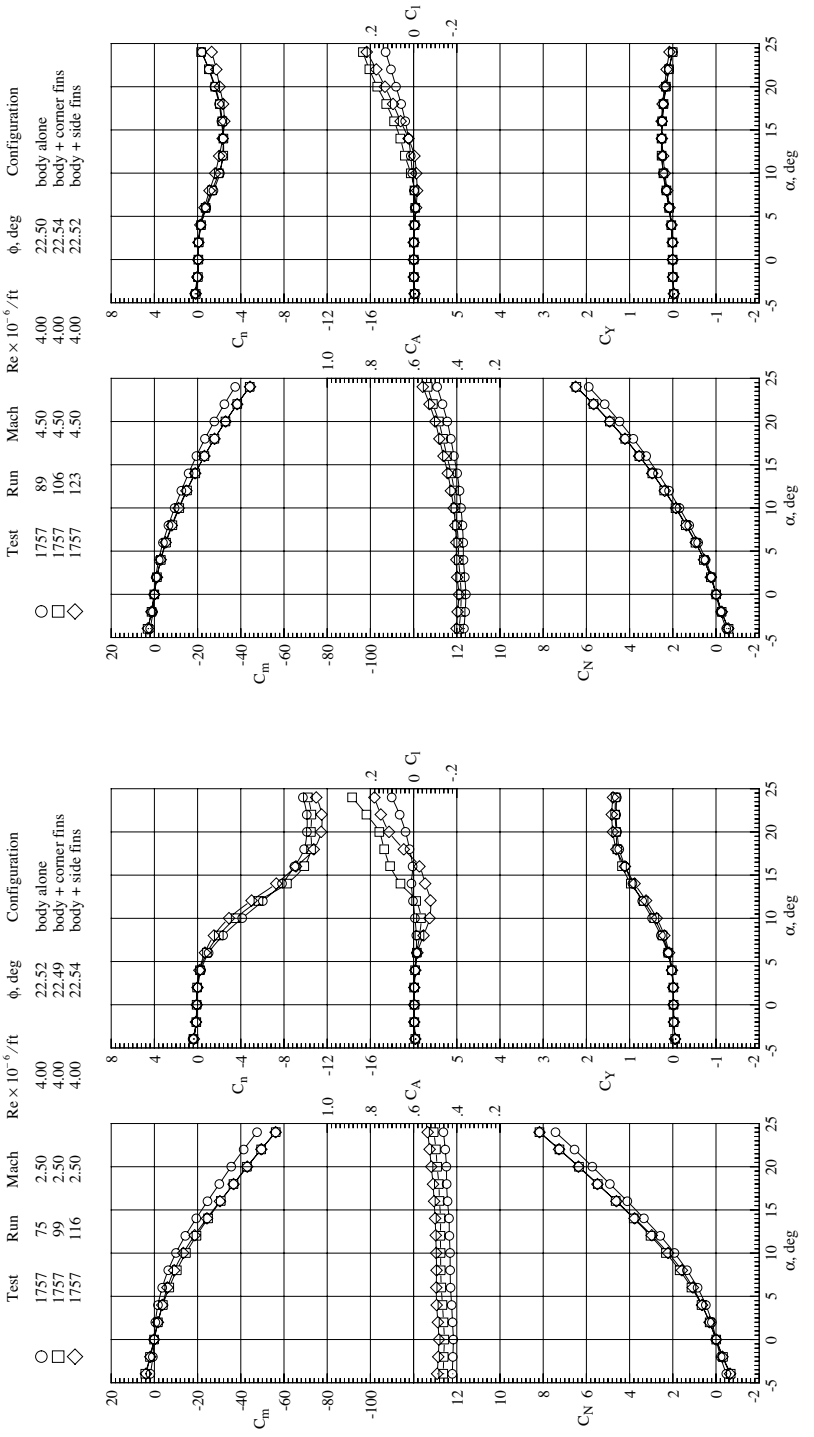

b. 22.5° roll.
Figure 12. Continued.

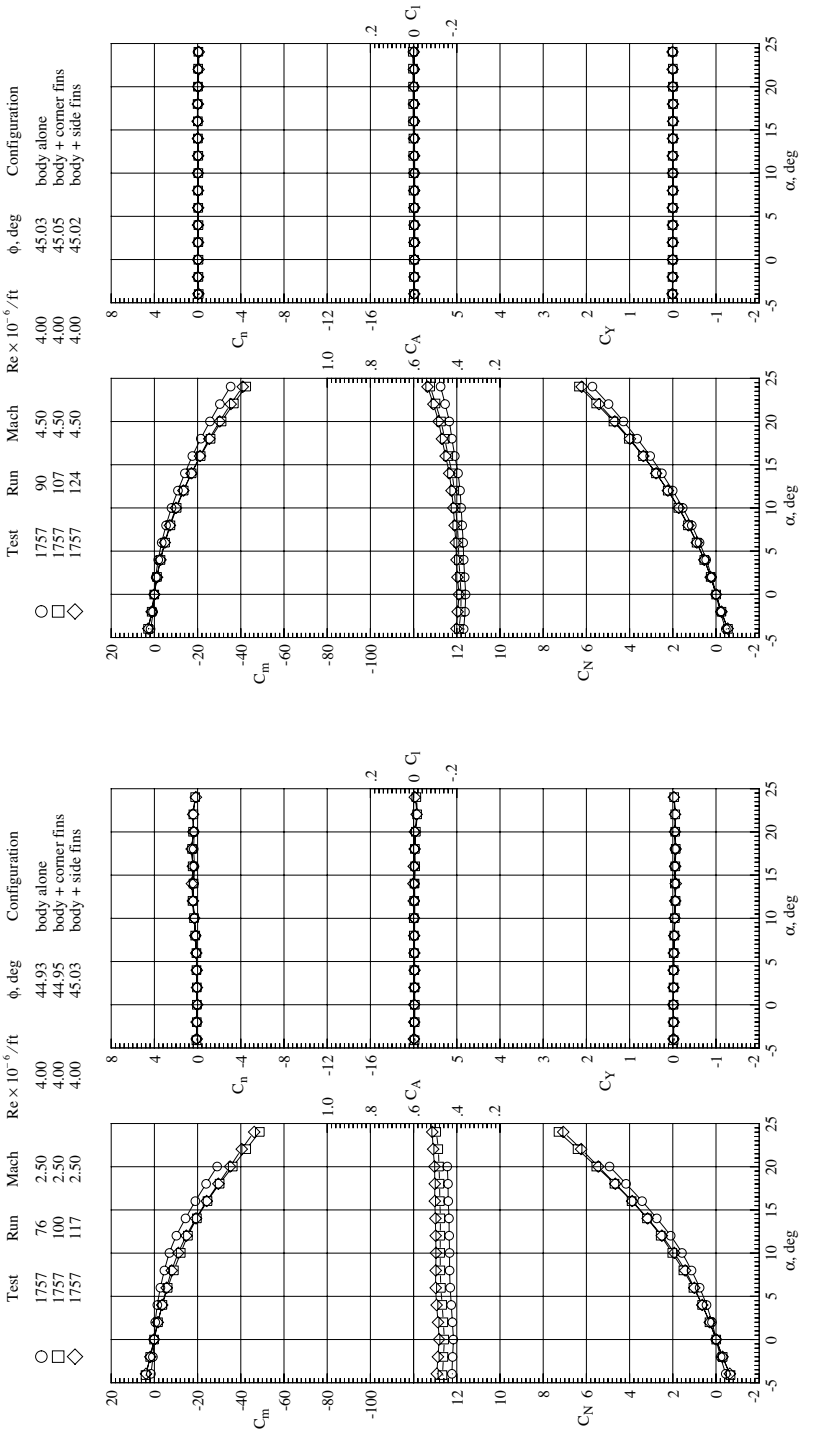

c. 45° roll.
Figure 12. Concluded.

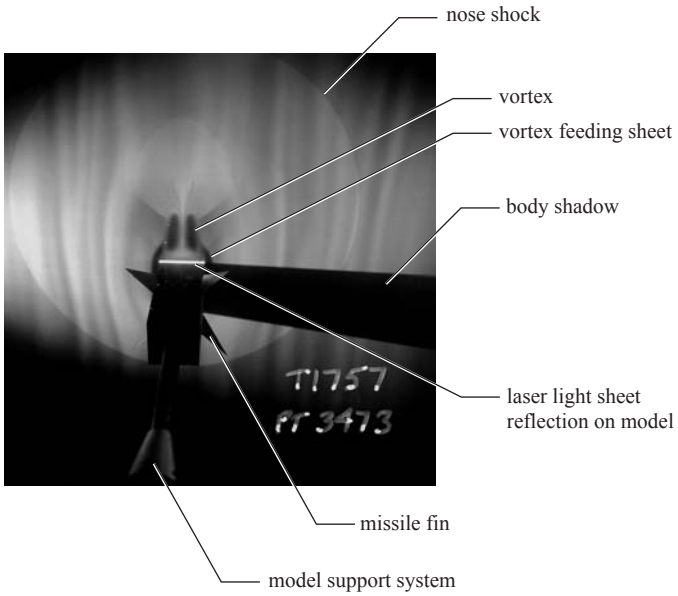

Figure 13. Sample vapor screen image.

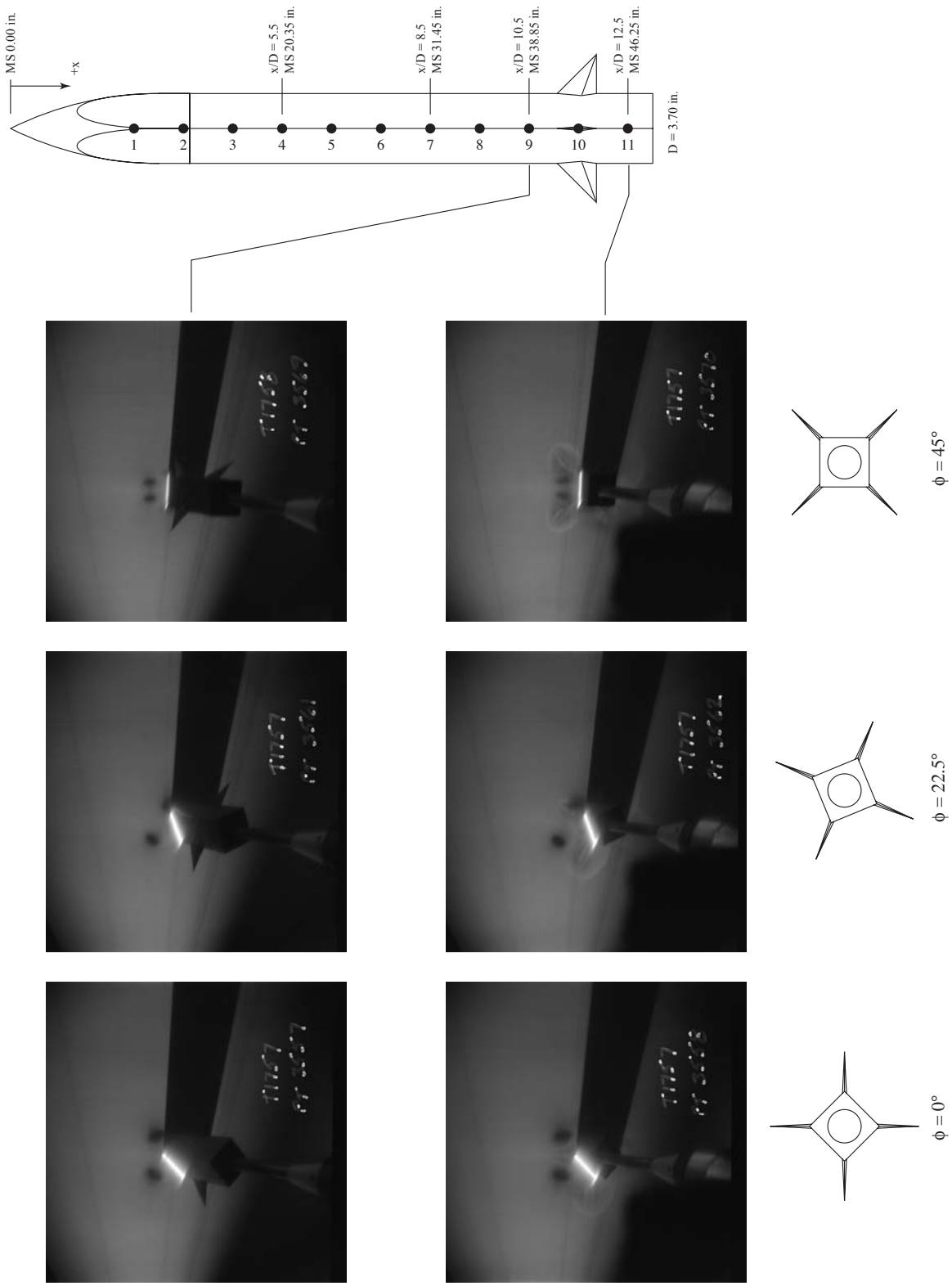

a. M = 2.50.

Figure 14. Vapor screen images of body with corner mounted tail fins at α = 14°.

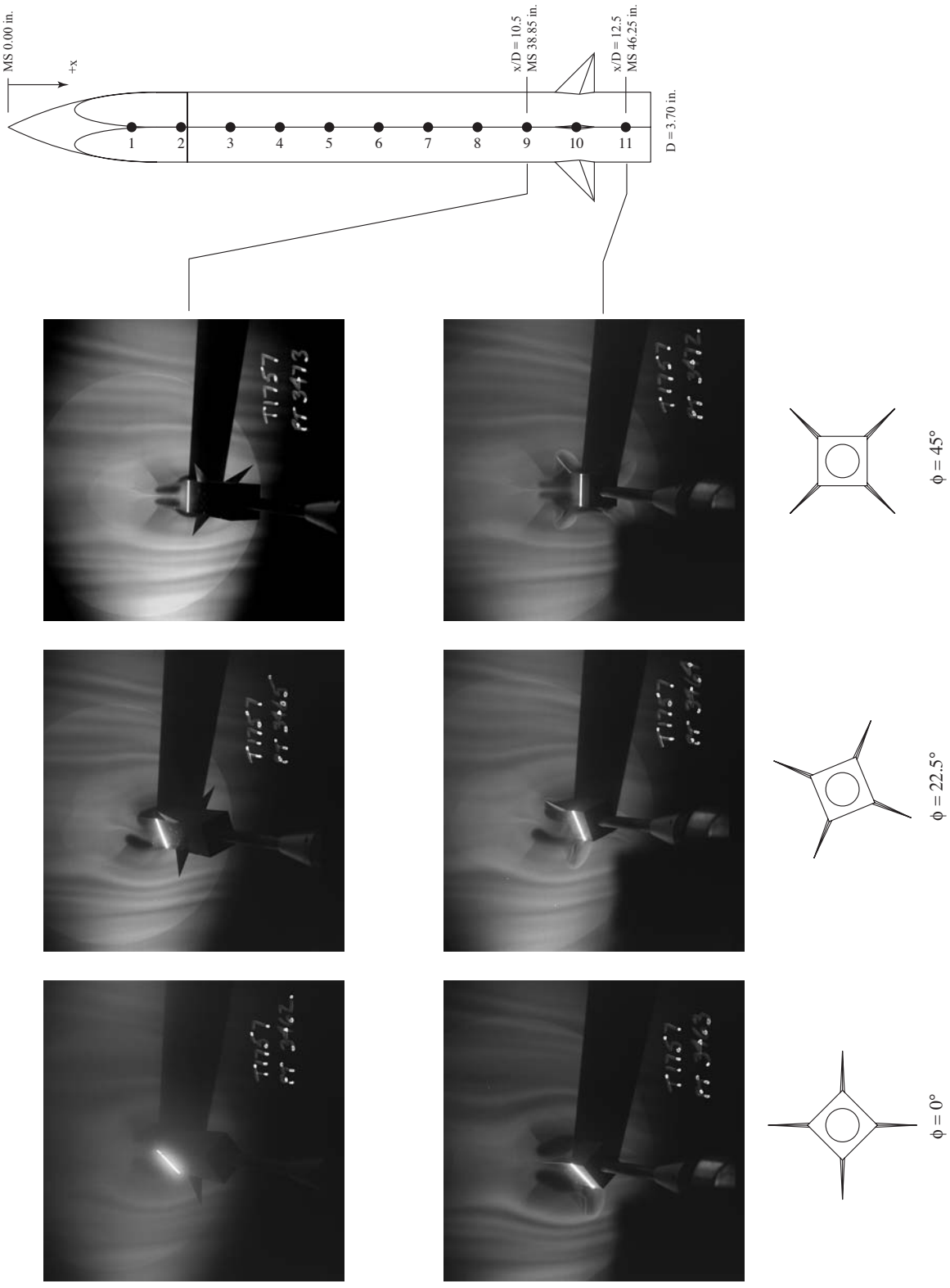

b. M = 4.50.

Figure 14. Concluded.

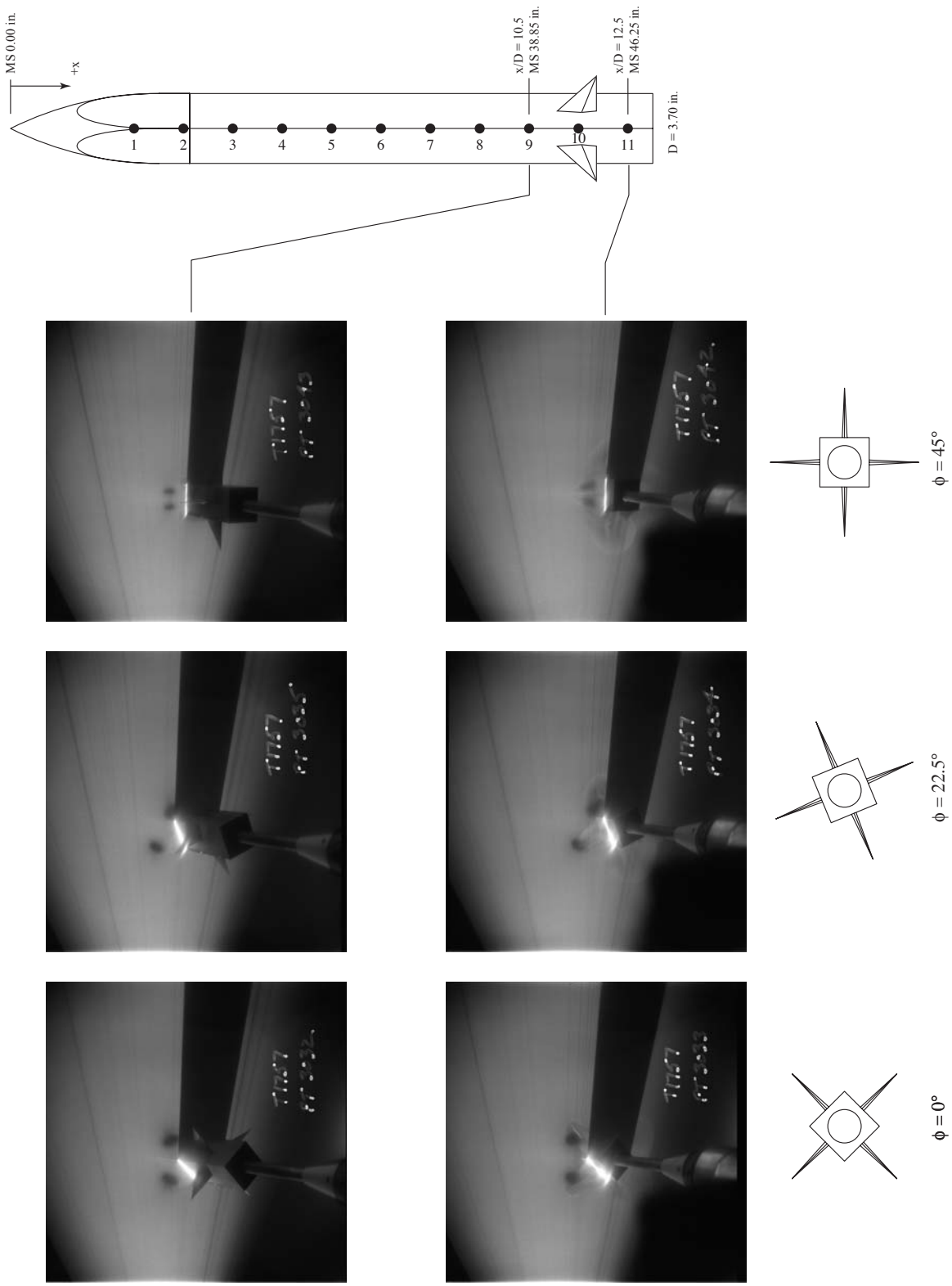

a. M = 2.50.

Figure 15. Vapor screen images of body with side mounted tail fins at α = 14°.

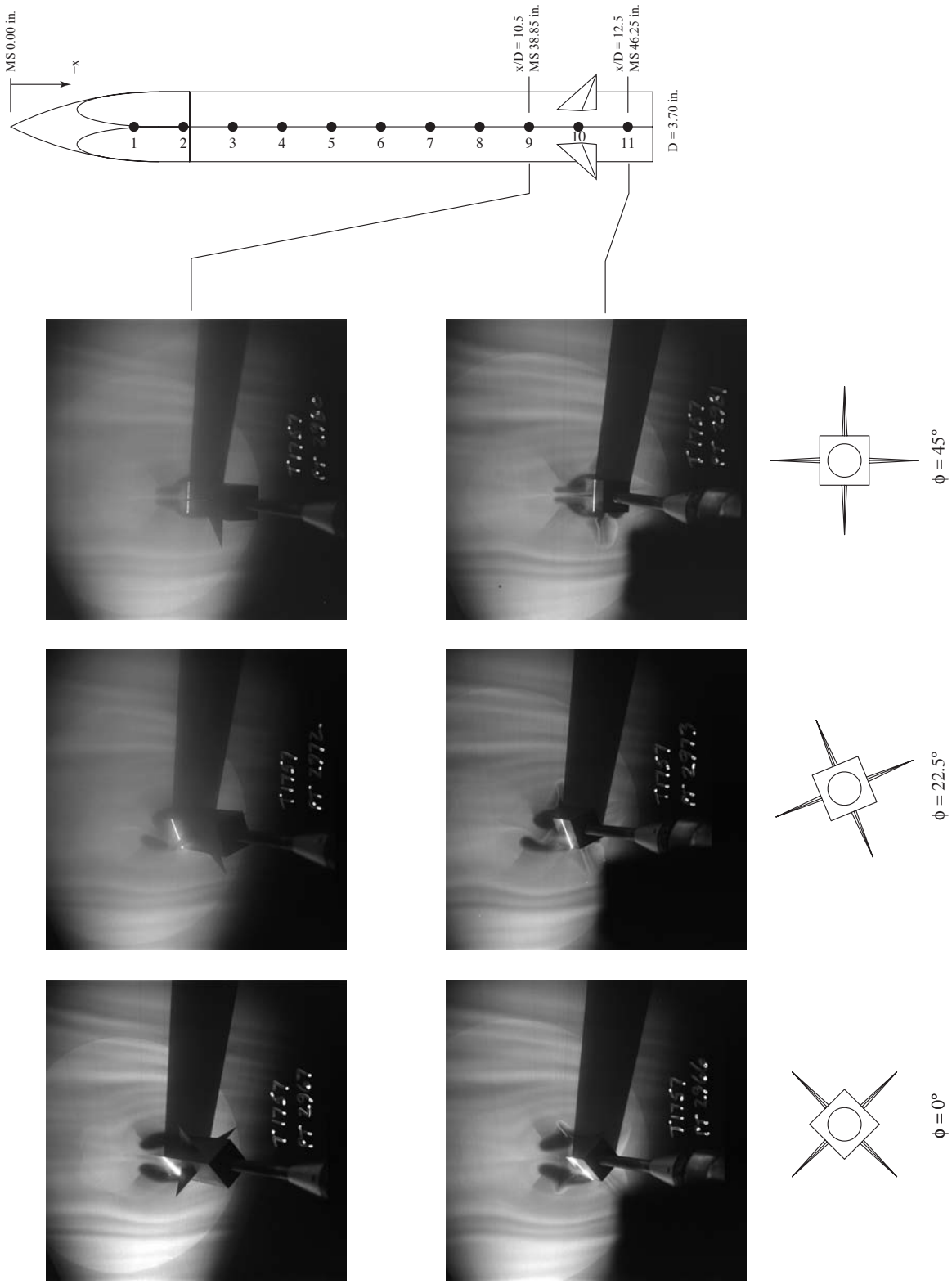

b. M = 4.50.
Figure 15. Concluded.